



A Journal of the Gesellschaft Deutscher Chemiker

Angewandte Chemie

GDCh

International Edition

www.angewandte.org

Accepted Article

Title: Fluorination Chemistry Enhances NIR-II Fluorescence of Polymer Dots for Quantitative Brain Tumor Imaging

Authors: Ye Liu, Jinfeng Liu, Dandan Chen, Xiaosha Wang, Zhe Zhang, Yicheng Yang, Lihui Jiang, Weizhi Qi, Ziyuan Ye, Shuqing He, Quanying Liu, Lei Xi, Yingping Zou, and Changfeng Wu

This manuscript has been accepted after peer review and appears as an Accepted Article online prior to editing, proofing, and formal publication of the final Version of Record (VoR). This work is currently citable by using the Digital Object Identifier (DOI) given below. The VoR will be published online in Early View as soon as possible and may be different to this Accepted Article as a result of editing. Readers should obtain the VoR from the journal website shown below when it is published to ensure accuracy of information. The authors are responsible for the content of this Accepted Article.

To be cited as: *Angew. Chem. Int. Ed.* 10.1002/anie.202007886

Link to VoR: <https://doi.org/10.1002/anie.202007886>

Fluorination Chemistry Enhances NIR-II Fluorescence of Polymer Dots for Quantitative Brain Tumor Imaging

Ye Liu,^[a] Jinfeng Liu,^[a] Dandan Chen,^[b] Xiaosha Wang,^[a] Zhe Zhang,^[b] Yicheng Yang,^[b] Lihui Jiang,^[a] Weizhi Qi,^[b] Ziyuan Ye,^[b] Shuqing He,^[b] Quanying Liu,^[b] Lei Xi,^[b] Yingping Zou,^{*[a]} Changfeng Wu^{*[b]}

[a] Dr. Y. Liu, J. Liu, X. Wang, Prof. L. Jiang, Prof. Y. Zou
College of Chemistry and Chemical Engineering, Molecular Imaging Research Center
Central South University
Changsha 410083, China
E-mail: yingpingzou@csu.edu.cn

[b] Dr. D. Chen, Z. Zhang, Y. Yang, W. Qi, Z. Ye, Prof. S. He, Prof. Q. Liu, Prof. L. Xi, Prof. C. Wu
Department of Biomedical Engineering
Southern University of Science and Technology
Shenzhen, Guangdong 518055, China
E-mail: wucf@sustech.edu.cn

Supporting information for this article is given via a link at the end of the document.

Abstract: Fluorescent probes in the second near-infrared region (NIR-II, 1000~1700 nm) have resulted in unprecedented imaging performance. Here, we describe a fluorination strategy in semiconducting polymers for development of highly bright NIR-II probes. Notably, tetrafluorination yielded a fluorescence QY of 3.2% for the polymer dots (Pdots), over 3-fold enhancement as compared to non-fluorinated counterparts. The fluorescence enhancement was attributable to nanoscale fluorine effect in the Pdots that maintained the molecular planarity and minimized the structure distortion between the excited state and ground state, thus reducing the nonradiative relaxations. Followed by through-skull and through-scalp imaging of the brain vasculature of live mice, we quantitatively analyzed the vascular morphology of transgenic brain tumors in terms of the vessel lengths, vessel branches, and vessel symmetry, which showed statistically significant differences from the wild type animals. The bright NIR-II Pdots achieved by fluorination chemistry provide insightful information for precise diagnosis of the malignancy of the brain tumor.

Introduction

Fluorescence techniques are leading to a rapid proliferation of advanced diagnostic tools in biomedicine.^[1] In particular, *in vivo* fluorescence imaging has resulted in significant advances in our understanding of various physiological processes and disease development.^[2] Recent research efforts have revealed a promising imaging window in the second near-infrared wavelength region (NIR-II, 1000~1700 nm). Reduced photon scattering in this spectral region allows fluorescence imaging at a significantly enhanced penetration depth and high signal-to-noise ratio as compared to the traditional wave-length region (400~900 nm).^[3] In a pioneer study, Dai and co-workers utilized the NIR-II photoluminescence of single-walled carbon nanotubes in a non-invasive through-skull brain imaging, which resolved cerebral vasculatures at a high spatial resolution of sub-10 μm and a depth of >2 mm in an epifluorescence imaging mode.^[4] Because of the unprecedented imaging quality, there is a great deal of attention in the development of various NIR-II fluorophores, including quantum dots (QDs),^[5] lanthanide nanoparticles,^[6] and organic fluorophores.^[7] However, the

intrinsic limitations of the current NIR-II probes, such as low absorptivity and poor quantum yields (QYs) have become the bottleneck in further development of high-contrast *in vivo* imaging techniques.

Semiconducting polymer dots (Pdots) exhibit optical properties such as high fluorescence brightness, fast emission rate, good photostability, and nontoxic features.^[8] The superior properties of Pdots over other fluorescent probes have established their potential in biology and medicine as very bright *in vitro* and *in vivo* probes.^[9] However, semiconducting polymers are weakly fluorescent in the NIR-II region. Moreover, the Pdots in aqueous solutions exhibit severe fluorescence quenching because the strong interchain interactions lead to energy funneling to low-energy chromophores.^[10] Recently, we reported a molecular engineering strategy towards the development of NIR-II fluorescent Pdots by managing aggregation-induced emission (AIE) of the polymer backbone and minimizing aggregation-caused quenching (ACQ) with steric hindrance of side-chain groups.^[11] Despite the progresses, the development of semiconducting polymers with bright fluorescence in the NIR-II window remains challenging.

Fluorination of semiconducting polymers has emerged as a powerful strategy for fine-tuning their physical and chemical properties.^[12] With large Pauling electronegativity and a small van der Waals radius, fluorine as a substituent in π -conjugated backbones can exert a great impact on the morphology and optical properties of the fluorinated semiconducting polymers. Significant effects discovered include lowering the molecular energy levels, enhancing intermolecular charge transfer (ICT), improving the molecular planarity, and affecting the orientation of polymer chains in the thin films.^[13] Because of these important factors, many peculiar properties of such fluorinated semiconducting polymers have been disclosed.^[14] The Pdots consist of densely packed polymeric chromophores, thus exhibiting chain-chain interactions and photophysical properties that resemble those in thin-film devices. The fluorination strategy in organic electronics is indicative of viable opportunities for enhancing the fluorescence of Pdot probes. For instance, Chiu and co-workers developed a highly fluorescent Pdots with a QY up to 49% in the visible region, which was 8 times brighter than its non-fluorinated counterpart.^[15] However, such effects are largely unexplored for semiconducting polymers in NIR-II region.

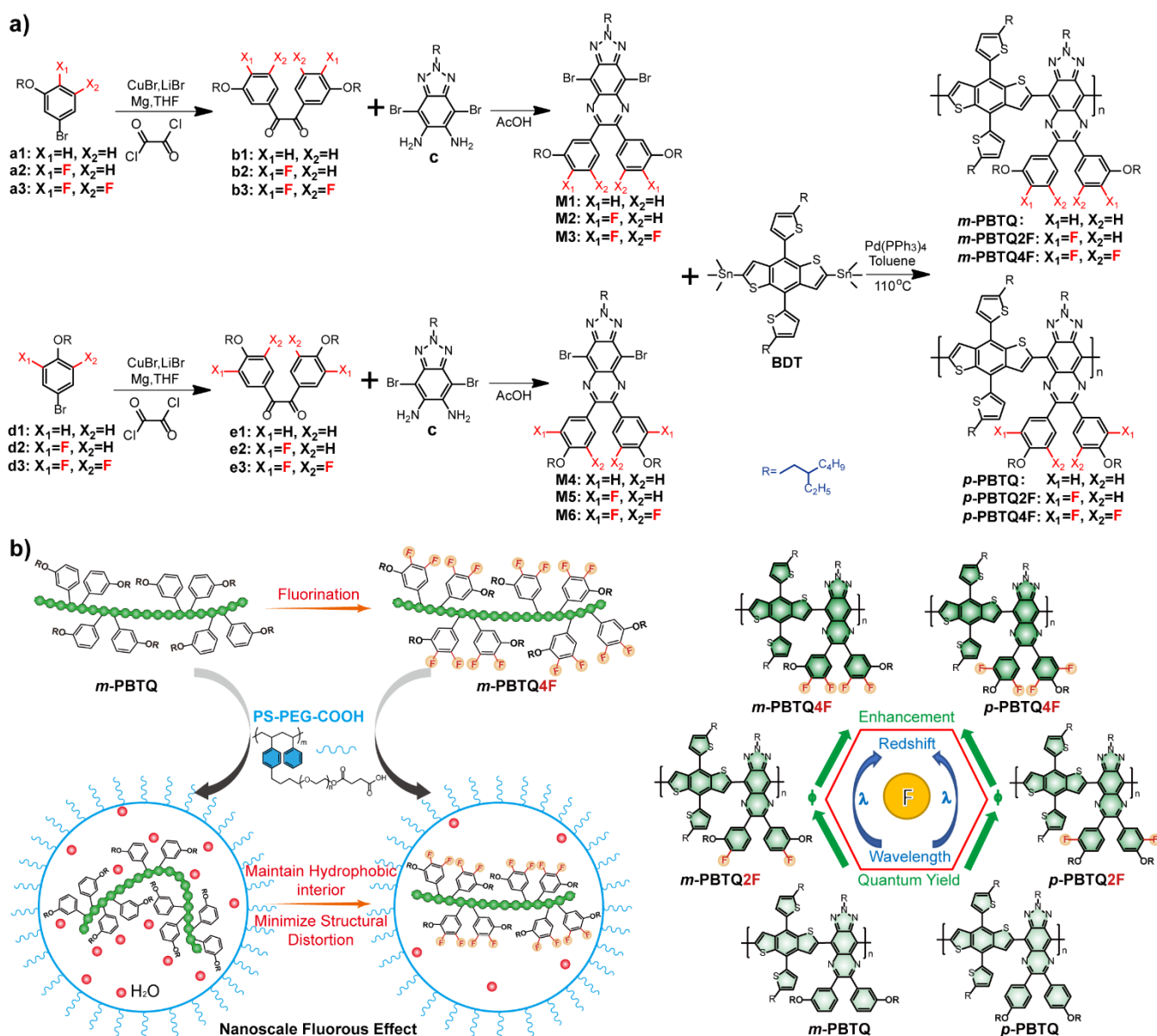


Figure 1. (a) Synthetic routes and fluorination strategy of semiconducting polymers. Fluorination was performed by varying the number and position of the fluorine substituent on the TQ acceptor of the semiconducting polymers. (b) Schematic illustration of nanoscale fluorine effect to maintain hydrophobic interior and minimize structure distortion of the Pdots. The fluorination redshifts the optical spectra and enhances the fluorescence quantum yield.

Here, we describe a fluorination strategy for development of highly fluorescent polymers in the NIR-II window. We designed two sets of fluorine substituted semiconducting polymers by using benzodithiophene (BDT) and triazole[4,5-g]-quinoxaline (TQ) derivatives used as donor and acceptors, respectively. We examined the effect of fluorination on the NIR-II fluorescence of the polymers as a function of the number and position of fluorination on the acceptor unit, aiming to outline a clear understanding of the benefits of the fluorine substitution. We discovered that fluorination significantly enhanced the fluorescence of Pdots in aqueous solution, which can be attributable to the nanoscale fluorine effect in the fluorinated Pdots. Density functional theory reveals that fluorination minimizes the structure distortion between the excited-state and

ground-state, thus reducing the nonradiative relaxations. Finally, we use the Pdots to demonstrate *in vivo* fluorescence imaging of the brain-tumor vasculature through the mouse skull, which showed a remarkable improvement in penetration depth and signal to background ratio (SBR). These results indicate that the fluorination strategy holds promise for development of highly fluorescent NIR-II fluorophores.

Results and Discussion

Molecular design and fluorination of semiconducting polymers. There have been recent efforts in the development of NIR-II organic fluorophores by judicious selection of building

blocks and side-chain engineering to form π -conjugated molecules.^[16] In this study, we explore the fluorination strategy in semiconducting polymers to obtain bright NIR-II probes. We start from two polymers with a donor-acceptor structure, in which BDT and TQ derivatives were used as donor and acceptors, respectively. The semiconducting polymers synthesized from BDT and TQ monomers can emit weak fluorescence in the NIR-II region.^[9b] The large π -conjugated backbones in these polymers provide several optional positions for fluorine substituents in the acceptor units. As fluorination of the acceptor unit is the most adopted strategy for donor-acceptor polymers,^[13] we examine the effect of fluorination on NIR-II fluorescence by

varying the number and position of the fluorine substituent on the TQ acceptor. In the TQ unit, the alkoxy chains anchored on the meta-position of benzene can provide different levels of hydrophobicity and steric hindrance as compared to the alkoxy chains anchored on the para-position of benzene. Therefore, we performed fluorination in the two types of acceptor structures. As shown in **Figure 1a**, we designed and synthesized six polymers, namely *m*-PBTQ, *m*-PBTQ2F, *m*-PBTQ4F polymers with the alkoxy chains anchored on the meta-position of benzene, and *p*-PBTQ, *p*-PBTQ2F, *p*-PBTQ4F polymers with alkoxy chains anchored on the para-position of benzene.

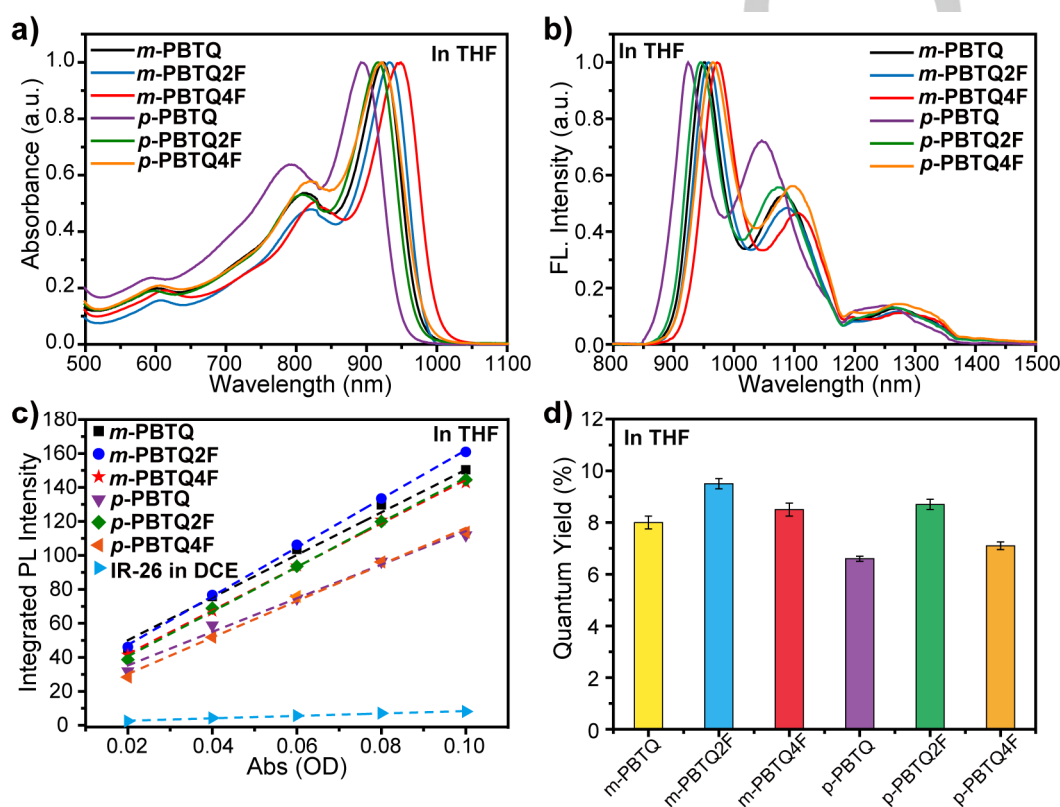


Figure 2. (a) Absorption spectra of the semiconducting polymers in THF solutions. (b) Fluorescence emission spectra of the polymers in THF. (c) Integrated fluorescence intensity plotted as a function of OD at 808 nm for the polymers in THF and IR-26 in 1,2-dichloroethane. (d) Quantum yields of the semiconducting polymers in THF solutions.

We rationalize that the fluorination of PBTQ polymers can effectively modulate the optical properties of the resulting Pdots, including the energy level lowering and fluorescence enhancement, in multiple manners (**Figure 1b**). Because of the strength of the C-F bond, fluorinated compounds show a high thermal and oxidative stability, high hydrophobicity, weak intermolecular interactions, and a small surface tension as compared to their non-fluorinated counterparts.^[17] These factors can enable the Pdots to maintain a hydrophobic interior and reduce chain-chain interactions. Because fluorination also increases the planarity of the conjugated backbone, thus suppressing the formation of bending or kinking of the polymer chains. Taken together, the fluorination strategy can provide a viable approach for enhancing the NIR-II fluorescence of Pdots.

The fluorination of the semiconducting polymers were designed and implemented according to the synthetic strategy

described in **Scheme S1**. The diketone compounds (**b1/b2/b3/e1/e2/e3**) were synthesized by non-fluorine (**a1/d1**) or fluorine-substituted (**a2/a3/d2/d3**) benzene derivatives via Grignard reaction. Then, the TQ acceptors (**M1/M2/M3/M4/M5/M6**) were synthesized from the diketone compounds and organic amine (**c**) dehydration that formed a pyrazine ring. Finally, TQ acceptors and BDT were polymerized by the Stille coupling reaction. The detailed synthesis of monomers and polymers, general characterizations including optical spectroscopy (**Figure S1-S7**), cellular assays (**Figure S8**), imaging data (**Figure S9-S11**), and NMR spectroscopy (**Figure S12-S39**) were provided in Supporting Information. The number average molecular weight (M_n) and polydispersity index (PDI) of the semiconducting polymers were measured by gel permeation chromatography (**Table S1**).

We investigated the optical properties of the semiconducting polymers in organic solvents. As shown by **Figure 2a** and **2b**, the absorption and emission spectra of polymers in THF were gradually red-shifted as the number of fluorine atoms on TQ increased. The absorption spectra of these polymers stride the traditional NIR-I window, which can be conveniently excited by an 808 nm laser. The fluorescence of the polymers covers the NIR-II spectral region, with their shoulder peaks extending beyond 1300 nm. The fluorescence QYs of these polymers in THF were determined by using IR26 dye as a reference (**Figure 2c**). The QYs of the six polymers varied from ~6.6% to ~9.5%, (**Figure 2d**), indicating that the fluorination has only minor effect on the fluorescence of the polymers in organic solvents. It is worth noting that the QY of ~9.5% was the highest among various NIR-II fluorophores, indicate that these polymers have great potential in the NIR-II imaging.

Fluorination enhanced fluorescence in Pdots. The Pdots were prepared from the semiconducting polymers according to a nanoprecipitation method described in previous reports.^[6a,18] A functional amphiphilic polystyrene polymer (PS-PEG-COOH) was used to form PEGylated Pdots. The resulting Pdots have a hydrodynamic diameter of ~22 nm, as determined by dynamic light scattering. The particle size and spherical morphologies of the Pdots were confirmed by transmission electron microscopy (**Figure 3a**). All the Pdots exhibited good colloidal stability in aqueous solutions for months. As shown by the optical spectroscopy (**Figure 3b** and **3c**), fluorination red-shifted the absorption and emission spectra of the Pdots, following the same trend as those for the polymers in THF. The absorption of the Pdots were normalized according to an optical density value of 0.1 at 808 nm (**Figure 3b**). Under the same excitation density at 808 nm, the fluorescence spectra of the Pdots were shown in **Figure 3c**. In contrast with the similar fluorescence intensities for the polymers in THF solutions, the fluorinated Pdots showed significantly enhanced fluorescence as compared to the non-fluorinated counterparts. Impressively, the *m*-PBTQ Pdots series exhibited higher QYs than the *p*-PBTQ Pdots series, and in each series, the QYs of Pdots were greatly improved as the number of fluorine atoms on the acceptor increased. The tetrafluorinated *m*-PBTQ4F Pdots achieved a QY of ~3.2%, which was the highest reported so far for NIR-II Pdots. This value was over 3-fold higher than that of the non-fluorinated *m*-PBTQ Pdots (~1.0%) and 5-fold higher than that of non-fluorinated *p*-PBTQ Pdots (~0.6%).

We compared the imaging performance of the fluorinated Pdots with two organic dyes such as Indocyanine Green (ICG) and IR26. As shown in **Figure 3d**, NIR-II fluorescent images of IR26 (in DCE), ICG in water, and *m*-PBTQ4F Pdots in water were taken with the same weight concentration (100 µg/mL), which indicated the fluorescence signal of *m*-PBTQ4F Pdots was ~5 times brighter than that of ICG and ~4 times than IR26, respectively. Furthermore, the photostability of ICG in water, IR26 in dimethyl sulfoxide, and *m*-PBTQ4F Pdots in water with the same weight concentration (100 µg/mL) was examined under continuous laser excitation (808-nm laser, 1 W/cm²) for over 120 min (**Figure 3e**). In contrast to the poor photostability of ICG and IR26, which exhibited severe photodegradation and fluorescence decrease to ~20% in 20 min, the fluorescence of *m*-PBTQ4F Pdots retained ~80% of the initial intensity after 120-min laser illumination. These results indicate the superior

brightness and photostability of the *m*-PBTQ4F Pdots for fluorescence imaging in the NIR-II window.

Mechanistic study on fluorination enhanced fluorescence. The *m*-PBTQ and *p*-PBTQ polymers series in organic solvents present relatively high fluorescence QYs. However, the Pdots show fluorescence quenching in comparison with the original polymers in organic solvents. The quenching can be attributed to intense inter- and intra-chain interactions, whereas the bending or kinking of the polymer chains in Pdots result in the formation of non-emissive species.^[19] In addition, energy migration in the large π -conjugated systems may also lead to energy funneling to the non-emissive species, amplifying the fluorescence quenching effect. Both *m*-PBTQ and *p*-PBTQ polymer series show consistent variation trend in the fluorination enhanced fluorescence. While each polymer series in organic solvents show only minor changes, the resulting Pdots exhibit significantly different QYs owing to fluorination. Most probably, fluorous effect plays an important role in the enhanced fluorescence of the Pdots. Fluorous effect can be described as the tendency of fluorinated compounds to segregate in order to favor fluorine-fluorine interactions, or more appropriately to avoid unfavored interactions with other elements.^[20] Presumably, the fluorination can lead to a hydrophobic nanoparticle interior as well as planar polymer conformation as compared to the nonfluorinated Pdots. **Figure S6** showed the absorption and fluorescence spectra of the *p*-PBTQ polymer series in THF solutions and the related Pdots in water, respectively. For the nonfluorinated *p*-PBTQ polymer, the absorption and fluorescence spectra of the Pdots in water were inhomogeneously broadened and the vibronic peaks were significantly increased as compared to those of the polymer in THF solutions. These results are consistent with previous studies that the increased conformational disorder in conjugated polymers increased the inhomogeneous spectral broadening and enhanced the 0-1 intensity relative to the 0-0 intensity.^[21] In contrast, the tetrafluorinated *p*-PBTQ4F Pdots show slightly redshifted absorption and fluorescence with only minor increase in vibronic peaks as compared to those of the polymer in THF solutions. The *m*-PBTQ4F Pdots showed similar spectral shape to those of the polymer in THF solution (**Figure S7**). These spectroscopic results support the presumption that the fluorination leads to planar polymer conformation and reduce conformational disorder during formation of the Pdots.

The QY ratios of the Pdots relative to the polymers in THF were plotted in **Figure 3f**, which measures the extent of fluorescence quenching in Pdots. As indicated, the value of *m*-PBTQ4F (~0.38) was over 3-fold higher than that of *m*-PBTQ (~0.12), whereas the value of *p*-PBTQ4F (~0.21) was over 2-fold higher than that of *p*-PBTQ (~0.09), indicating that the fluorescence of the *m*-PBTQ4F polymer was largely retained in the Pdots with only moderate quenching. It is surprising to observe the QY of the *m*-PBTQ4F Pdots (~3.2%) was over 2 times higher than that of the *p*-PBTQ4F (~1.5%) despite their similar QYs for the polymers in THF solution. This is an additional evidence for fluorous effect as the four fluorine atoms in *m*-PBTQ4F are in proximity to each other, thus collectively enabling a strong repulsion to water and chain-chain aggregation. Because of the fluorous effect, the hydrophobicity and molecular planarity of the polymer are largely retained in the Pdots, suppressing the quenching by the inter-chain interactions and non-emissive species.

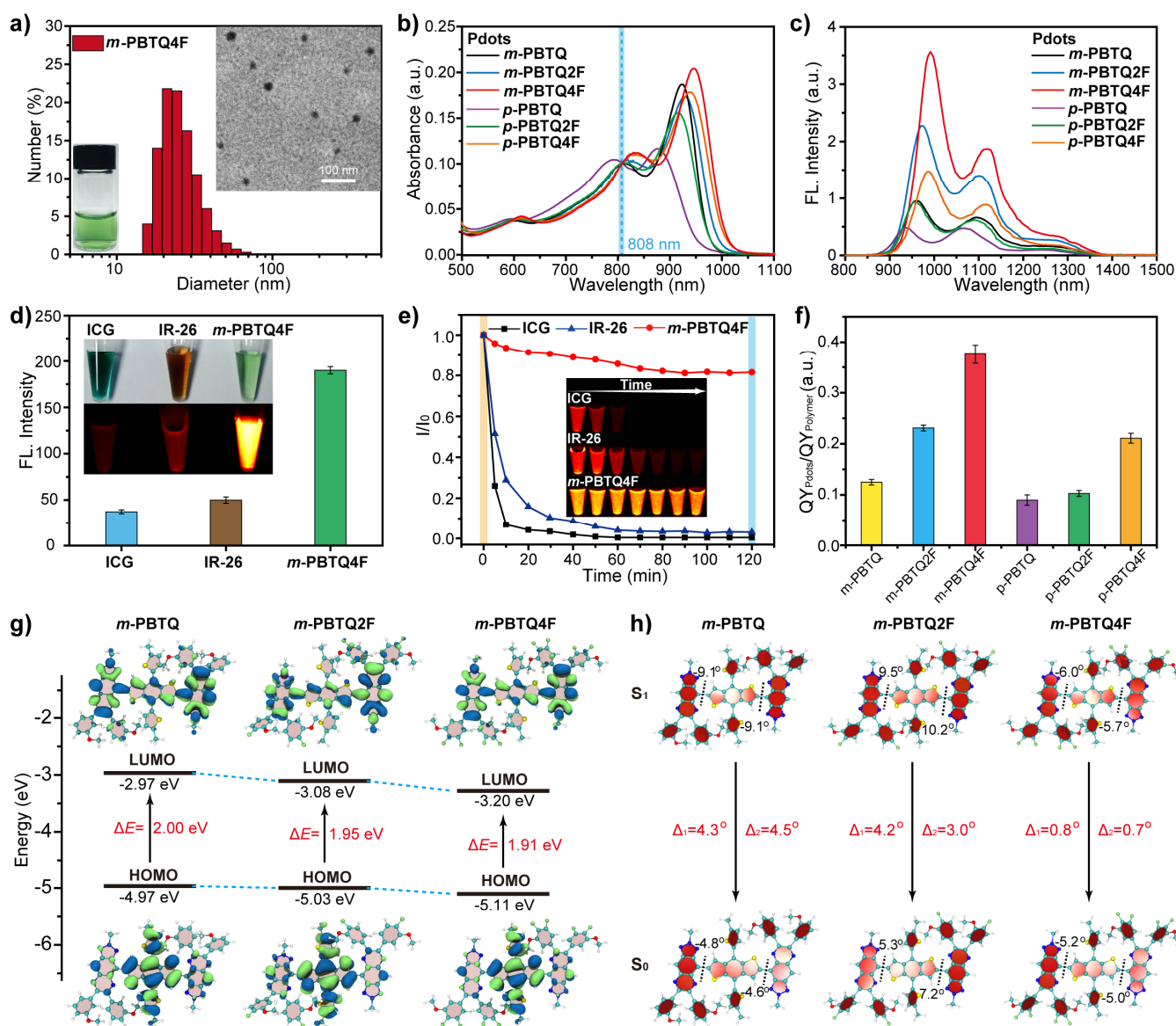


Figure 3. (a) Hydrodynamic diameter distribution of the *m*-PBTQ4F Pdts measured by dynamic light scattering. The insets show a typical transmission electron microscope image of the *m*-PBTQ4F Pdts and photograph for *m*-PBTQ4F Pdts solution at 100 $\mu\text{g/mL}$ concentration. (b) Absorption spectra of the Pdts with the optical density of 0.1 at 808 nm. (c) Fluorescence spectra of the Pdts measured with the same excitation density at 808 nm. (d) The mean fluorescence intensity of ICG in water, IR-26 in 1,2-dichloroethane, *m*-PBTQ4F Pdts in water with the same mass concentration (100 $\mu\text{g/mL}$) (30 mW/cm^2 , 808 nm laser, 1000 nm LP filter). The insets show the corresponding photograph and NIR-II fluorescent images. (e) Photostability of ICG in water, IR-26 in dimethyl sulfoxide, and *m*-PBTQ4F Pdts in water with the same mass concentration (100 $\mu\text{g/mL}$) under continuous 808 nm radiation (1 W/cm^2) for 120 min. I/I_0 represents the ratio of the fluorescence intensity of the samples relative to the initial intensity. The inset shows the corresponding NIR-II fluorescent images. (f) The ratios of the quantum yields of the Pdts relative to the polymer in THF solutions. (g) Theoretical calculation results of the HOMOs and LUMOs of *m*-PBTQ series. (h) Optimized S_0 and S_1 geometries and the dihedral angles for the *m*-PBTQ series by density functional theory.

To elucidate the fluorination enhanced fluorescence, we carried out theoretical calculations regarding the energy levels and molecular geometries of *m*-PBTQ series by using density functional theory (DFT) and time-dependent density functional theory (TDDFT). In the calculation, we calculate only one repeating-unit (A-D-A) in water owing to the limit of computation power. As shown in **Figure 3g**, all the HOMOs are mainly located on the BDT donor, and the LUMOs are mainly localized on the TQ acceptor. Additionally, both the HOMO and LUMO energy levels were reduced by increasing the number of fluorine atoms on the TQ unit. It indicates that the fluorination could

effectively lower the HOMO and LUMO energy levels of the polymers. The energy gaps (E_g) calculated from the HOMO and LUMO were 2.00 eV for *m*-PBTQ, 1.95 eV for *m*-PBTQ2F, and 1.91 eV for *m*-PBTQ4F, respectively. This is consistent with the experimental results by spectroscopy that the fluorination could narrow the energy gap and red-shift both the absorption and emission spectra.

We further analyzed the molecular geometry structures to better understand the fluorination enhanced fluorescence. The energy gap law dictates that as the emission wavelength shifts to the red, the nonradiative decay of the excited state becomes

more dominant.^[22] To decrease the nonradiative decay rate, the structural distortion between the emitting excited-state and the ground-state must be minimized.^[23] Besides the probable suppression of non-emissive species, fluorination may reduce the structure distortion between the excited and ground states to enhance the emission QY of the Pdots. We computed the ground-state (S_0) and first singlet excited-state (S_1) geometries of the *m*-PBTQ series (Figure 3h). Considering A-D-A unit, two dihedral angles were calculated in terms of the left and the right acceptor relative to the middle donor. For both S_0 and S_1 geometries, the dihedral angles Φ_L (dihedral angle between the left acceptor and middle donor) and Φ_R (dihedral angle between

the right acceptor and middle donor) were computed and summarized in Table S2. As seen clearly, the differences (Δ values) in the dihedral angles between S_0 and S_1 were determined to be 4.3° and 4.5° for *m*-PBTQ, 4.2° and 3.0° for *m*-PBTQ2F, and 0.8° and 0.7° for *m*-PBTQ4F, respectively. As the number of fluorine atoms increased, the Δ values apparently decreased, indicating reduced structure distortion between S_0 and S_1 state for the tetrafluorinated *m*-PBTQ4F as compared to non-fluorinated *m*-PBTQ. Taken together, the structural distortion between the excited-state and the ground-state was minimized by fluorination, thereby decreasing the nonradiative decay rates and enhancing the emission QY.

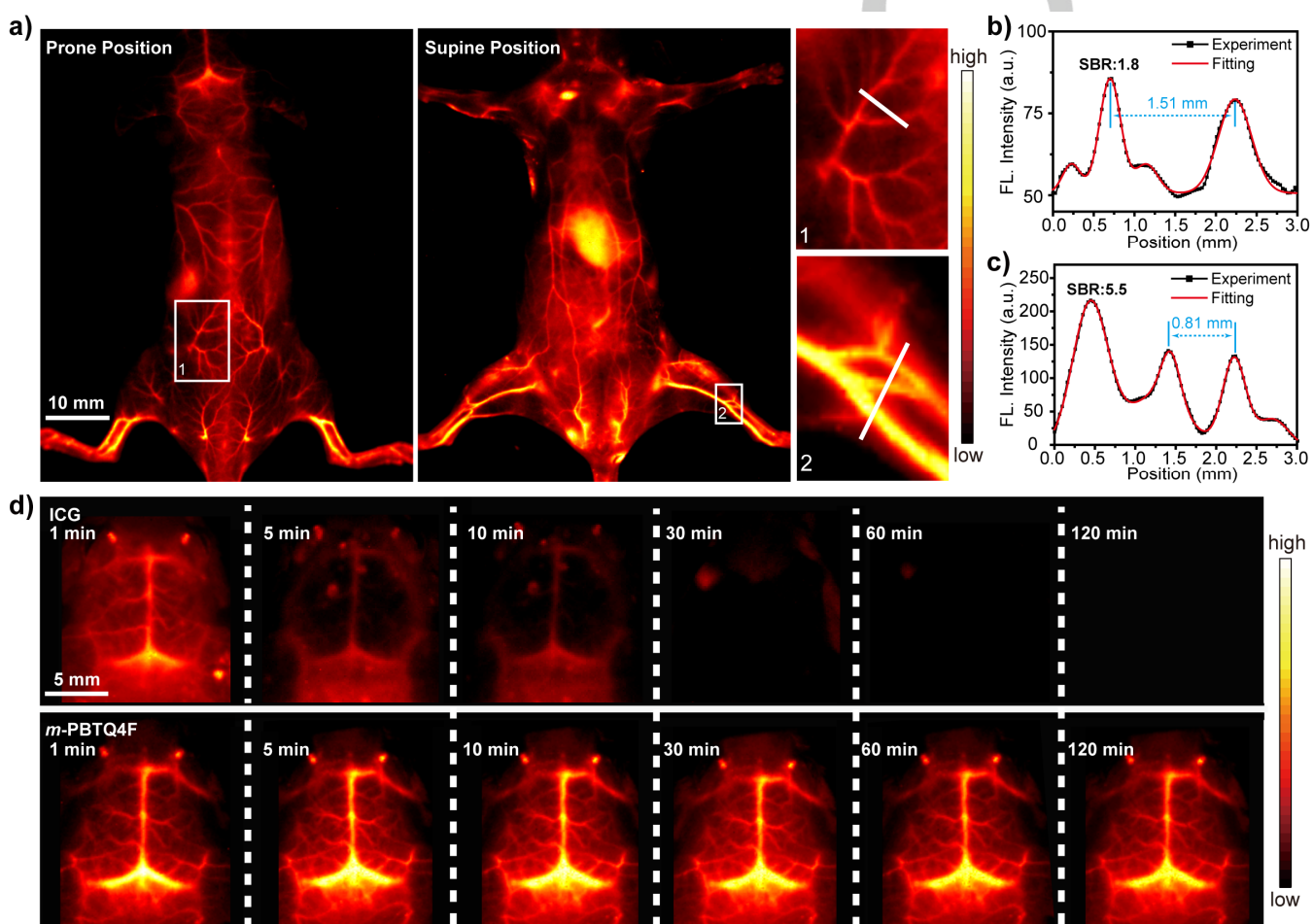


Figure 4. (a) *In vivo* NIR-II whole-body fluorescence imaging of C57BL/6 mice in prone and supine positions after tail-vein injection of 100 μ L *m*-PBTQ4F Pdots (200 μ g/mL). (b) and (c) show the cross-sectional fluorescence intensity profile measured along the white line and Gaussian fits (red) in (a)-1 and (b)-2, respectively. (d) *In vivo* NIR-II fluorescence imaging of cerebral vasculature of C57BL/6 mice injected with 100 μ L ICG or *m*-PBTQ4F Pdots (200 μ g/mL) at certain time intervals from 1 to 120 min. (70 mW/cm², 808 nm laser, 1319 nm LP filter)

Quantitative through-skull imaging of brain vasculature. We performed *in vivo* fluorescence imaging in the NIR-II window by using the *m*-PBTQ4F Pdots in view of their high brightness and good photostability. We first examined the cytotoxicity of Pdots by measuring cell viabilities at various concentrations (0–100 μ g/mL) in MTT assays. As shown in Figure S8, the cell viability after 24 h incubation was over 90% even in the high Pdot concentration (100 μ g/mL), indicating good biocompatibility of Pdots with cells. Next, we evaluated the *in vivo* whole-body fluorescence imaging of *m*-PBTQ4F Pdots in live mice. Low

excitation density (70 mW/cm²) by a 808 nm laser was adopted to reduce damage to the mice while maintaining image quality. C57BL/6 mice were administered with the Pdots through the tail vein (100 μ L, 200 μ g/mL). We identified that the imaging with a 1319 nm long-pass filter resulted in the best signal to noise ratio (Figure S9). As indicated in Figure 4a, the whole-body imaging of a mice in both supine and prone positions clearly show the vascular structures throughout the body. As expected, these images with tetrafluorinated *m*-PBTQ4F Pdots exhibited much higher signal-to-noise ratio (SNR) than those with non-

fluorinated *m*-PBTQ Pdots (Figure S10), confirming the superior performance achieved by the fluorination strategy. In the prone position, the images of the blood vessels in the mice's back (SBR=1.8) could be clearly observed (Figure 4b). The images of the blood vessels of the hindlimbs can reach a high SBR of 5.5, which is over 2-fold higher SBR (5.5 vs 2.4) than that of *m*-PBTQ Pdots. These results demonstrate that the fluorinated Pdots could offer high SBR and resolution in whole-body fluorescence imaging.

Recent studies demonstrated that fluorescence detection in the 1300–1400 nm region resulted in drastically improved SNR and penetration depth in deep-tissue imaging *in vivo*.^[4,11] We explore the application of the fluorinated Pdots for through-scalp and through-skull imaging of mice brain. We compared the performance of *m*-PBTQ4F Pdots and ICG dye in the imaging of mouse cerebral vasculature. The Pdots and ICG solution at the same injection dose (200 µg/mL, 100 µL) were administered into

C57BL/6 mice through the tail vein. Fluorescence images were taken through-scalp and through-skull of the mice at certain time intervals for 120 min (Figure 4d). As indicated, the fluorescence signal of the cerebral vasculature with ICG declined very fast, and almost disappeared in 5 min. In contrast, there was much higher SNR and resolution in the imaging of the vasculature with *m*-PBTQ4F Pdots, and it persisted for more than 2 h after Pdots injection because of their long blood circulation time. This could be advantageous for vascular imaging as well as imaging-guided surgery. At the first minute post injection, the fluorescence signal of *m*-PBTQ4F Pdots in the cerebral vasculature was much stronger than that of ICG. These results demonstrate that the performance of *m*-PBTQ4F Pdots, with long imaging duration, high SNR and spatial resolution, is superior to the clinically-approved imaging by ICG in the NIR-II window.

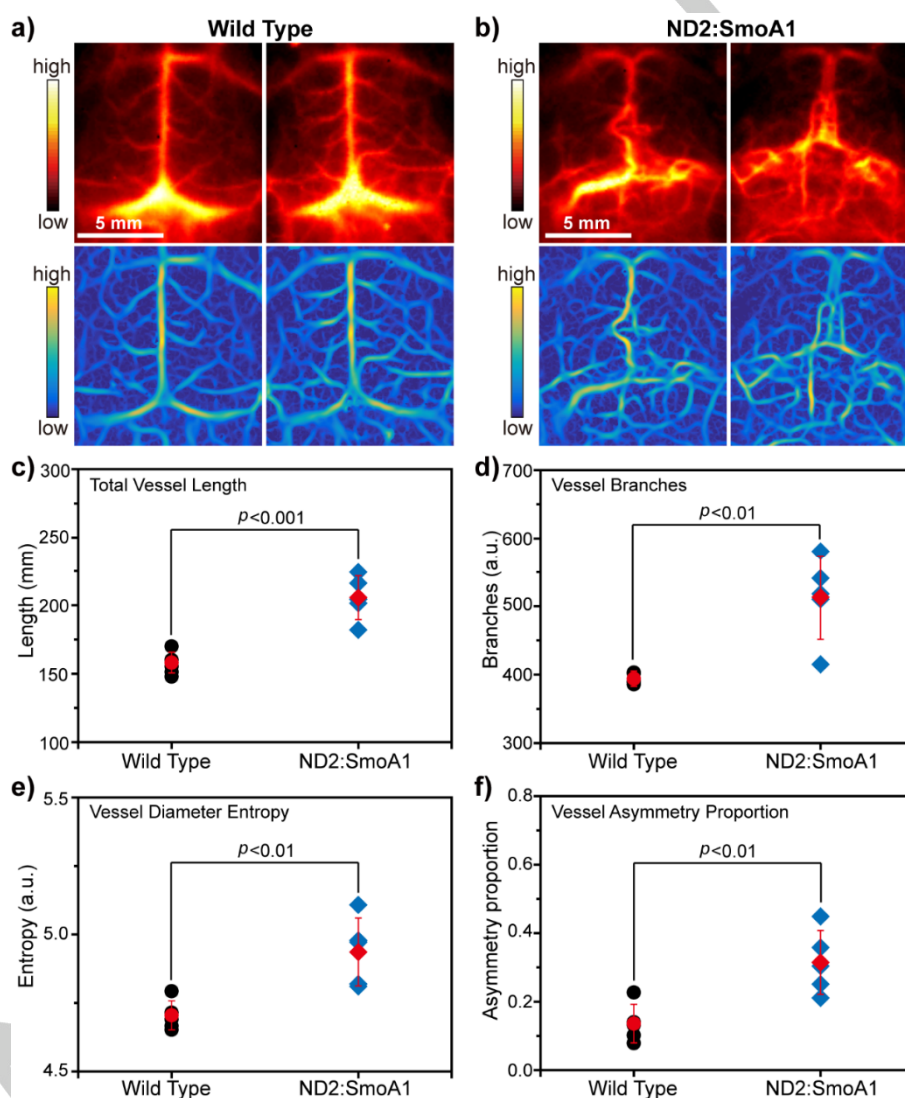


Figure 5. (a) *In vivo* NIR-II fluorescence images (top panel) and Hessian-matrix-enhanced images (bottom panel) of cerebral vasculature of wild-type C57BL/6 mice (n=5). (b) *In vivo* NIR-II fluorescence images (top panel) and Hessian-matrix-enhanced images (bottom panel) of cerebral vasculature of ND2:SmoA1 mice (n=5). (c-f) Quantitative imaging of vascular morphology of the mouse brain by using a vascular segmentation and quantification algorithm. The data are analyzed by two-sided Student's t test. Red data are reported as mean ± standard deviation.

Malignant brain tumors are characterized by a number of histopathological features including infiltrative growth, microvascular proliferation and pleomorphic vessels.^[24] Inspired by the imaging results of mouse cerebral vasculature, we attempt to explore the through-skull and through-scalp imaging of brain tumor vasculature by using the fluorinated Pdots. We chose a transgenic mouse model, ND2:SmoA1, because it closely resembles human medulloblastoma, the most common malignant childhood brain tumor.^[25] For comparative studies, we used five ND2:SmoA1 mice and five wild-type C57BL/6 mice, and two of each group was shown in **Figure 5** (the images of the other 3 mice were provided in **Figure S11**). As indicated by the through-skull imaging results, the brain vasculature in ND2:SmoA1 mice is structurally abnormal as compared to that of the wild-type animals. We can visually identify the significant difference between the normal and brain tumor group. Whereas the normal vasculature is arranged in a hierarchy of evenly spaced and well-differentiated blood vessels, the tumor vasculature is unevenly distributed and chaotic, exhibiting serpentine courses and irregular branches. These imaging results clearly reveal the vascular characteristics of medulloblastoma as compared to the wild-type animals.

Finally, we assess and quantify the vascular morphology of the mouse brain by using a vascular segmentation and quantification algorithm. Quantitative imaging of vascular morphology of the medulloblastoma not only generates multiple parameters regarding tumor angiogenesis, but also provides insightful information for precise diagnosis of the malignancy of the tumor. The vascular quantification algorithm is based on a modified Hessian matrix method.^[26] First, the original fluorescence images (Top panel in **Figure 5a** and **5b**) were processed to generate the Hessian-matrix-enhanced images (Bottom panel in **Figure 5a** and **5b**). Then, blood vessels were extracted from the enhanced images and the vascular centerlines were further identified. Finally, using the extracted image and the identified centerlines, the vascular morphological parameters, including the total vessel length (**Figure 5c**), the vessel branches (**Figure 5d**), and the vessel diameter entropy (**Figure 5e**), were computed. As seen from the **Figure 5a** and **5b**, the enhanced images agree well with the original images, but show much detailed vascular characteristics with high resolution. The parameter distributions calculated from the enhanced images indicate that the medulloblastoma mice have apparently higher values in terms of the total vessel length, the vessel branches, and the vessel diameter entropy as compared to the wild-type animals. Last, we applied a process pipeline to measure the asymmetry of vascular topography (**Figure 5f**), which indicated that the proportions of vascular asymmetry in the brain-tumor mice were obviously higher than those of the normal mice. Taken together, the multiple parameters calculated from the Hessian-matrix-enhanced images clearly outline the characteristics of medulloblastoma as compared to the wild-type mice. These results also high-light the great potential of the NIR-II Pdots combined with the quantitative through-skull imaging for early diagnosis of malignant brain tumors.

Conclusion

In summary, we have successfully demonstrated a fluorination strategy for development of bright fluorophores in NIR-II region.

The fluorine-substituted Pdots exhibit red-shifted emission and high fluorescence QY which are superior properties for deep-tissue NIR-II imaging. In one case, the QY of the tetrafluorinated **m-PBTQ4F** Pdots, with good photostability, reached up to 3.2% in aqueous solution, which was over 3-fold higher than that of the non-fluorinated counterparts and 6-fold higher than that of IR26. We postulate that the fluorination can result in planar polymer conformation and reduce chain-chain interactions in the fluorinated Pdots, which are consistent with the comparative spectroscopic studies for the polymer in THF solutions and Pdots in water. DFT calculations indicate that fluorination also minimize the structure distortion between the excited and ground states to enhance the emission QY of the Pdots. The fluorinated Pdots exhibited a remarkable improvement in penetration depth and signal to background ratio for deep tissue imaging, as confirmed by through-skull and through-scalp quantitative imaging of the brain-tumor vasculature of live mice. These results indicate that fluorination is a promising strategy for the design of highly fluorescence NIR-II fluorophores.

Acknowledgements

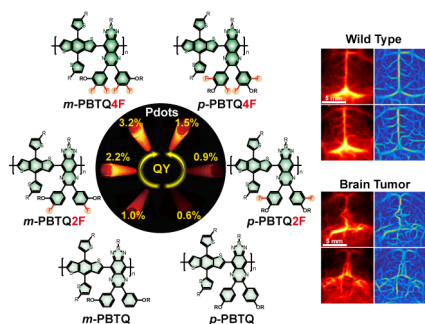
C. Wu acknowledges financial support from Shenzhen Science and Technology Innovation Commission (Grant No. KQTD20170810111314625) and the National Natural Science Foundation of China (Grant No. 81771930), and the National Key Research and Development Program of China (Grant No. 2018YFB0407200). Y. Zou acknowledges the National Natural Science Foundation of China (Grant No. 51673215), and Science Fund for Distinguished Young Scholars of Hunan Province (2017JJ1029).

Keywords: fluorination • fluorescent probes • polymer dots • NIR-II optical imaging • brain tumor

- [1] a) S. Kunjachan, J. Ehling, G. Storm, F. Kiessling, T. Lammers, *Chem. Rev.* **2015**, *115*, 10907-10937; b) D.-E. Lee, H. Koo, I.-C. Sun, J. H. Ryu, K. Kim, I. C. Kwon, *Chem. Soc. Rev.* **2012**, *41*, 2656-2672.
- [2] a) R. R. Zhang, A. B. Schroeder, J. J. Grudzinski, E. L. Rosenthal, J. M. Warram, A. N. Pinchuk, K. W. Eliceiri, J. S. Kuo, J. P. Weichert, *Nat. Rev. Clin. Oncol.* **2017**, *14*, 347; b) B. R. Smith, S. S. Gambhir, *Chem. Rev.* **2017**, *117*, 901-986.
- [3] a) G. Hong, A. L. Antaris, H. Dai, *Nat. Biomed. Eng.* **2017**, *1*, 1-22; b) S. Diao, J. L. Blackburn, G. Hong, A. L. Antaris, J. Chang, J. Z. Wu, B. Zhang, K. Cheng, C. J. Kuo, H. Dai, *Angew. Chem. Int. Ed.* **2015**, *54*, 14758-14762; c) S. Wang, J. Liu, G. Feng, L. G. Ng, B. Liu, *Adv. Funct. Mater.* **2019**, *29*, 1808365.
- [4] G. Hong, S. Diao, J. Chang, A. L. Antaris, C. Chen, B. Zhang, S. Zhao, D. N. Atochin, P. L. Huang, K. I. Andreasson, *Nat. Photonics* **2014**, *8*, 723.
- [5] a) G. Hong, J. T. Robinson, Y. Zhang, S. Diao, A. L. Antaris, Q. Wang, H. Dai, *Angew. Chem. Int. Ed.* **2012**, *51*, 9818-9821; b) G. Chen, F. Tian, Y. Zhang, Y. Zhang, C. Li, Q. Wang, *Adv. Funct. Mater.* **2014**, *24*, 2481-2488.
- [6] a) S. He, S. Chen, D. Li, Y. Wu, X. Zhang, J. Liu, J. Song, L. Liu, J. Qu, Z. Cheng, *Nano Lett.* **2019**, *19*, 2985-2992; b) H. Zhang, Y. Fan, P. Pei, C. Sun, L. Lu, F. Zhang, *Angew. Chem. Int. Ed.* **2019**, *131*, 10259-10263; c) M. Zhao, R. Wang, B. Li, Y. Fan, Y. Wu, X. Zhu, F. Zhang, *Angew. Chem. Int. Ed.* **2019**, *131*, 2072-2076.
- [7] a) Q. Miao, K. Pu, *Adv. Mater.* **2018**, *30*, 1801778; b) A. L. Antaris, H. Chen, K. Cheng, Y. Sun, G. Hong, C. Qu, S. Diao, Z. Deng, X. Hu, B. Zhang, *Nat. Mater.* **2016**, *15*, 235-242; c) S. Zhu, S. Herraiz, J. Yue, M.

- Zhang, H. Wan, Q. Yang, Z. Ma, Y. Wang, J. He, A. L. Antaris, *Adv. Mater.* **2018**, *30*, 1705799.
- [8] a) C. Wu, D. T. Chiu, *Angew. Chem. Int. Ed.* **2013**, *52*, 3086-3109; b) H.-S. Peng, D. T. Chiu, *Chem. Soc. Rev.* **2015**, *44*, 4699-4722; c) J. Li, J. Rao, K. Pu, *Biomaterials* **2018**, *155*, 217-235; d) L. Feng, C. Zhu, H. Yuan, L. Liu, F. Lv, S. Wang, *Chem. Soc. Rev.* **2013**, *42*, 6620-6633; e) Y. Jiang, J. McNeill, *Chem. Rev.* **2017**, *117*, 838-859; f) L. Jiang, H. Bai, L. Liu, F. Lv, X. Ren, S. Wang, *Angew. Chem. Int. Ed.* **2019**, *131*, 10770-10775.
- [9] a) G. Hong, Y. Zou, A. L. Antaris, S. Diao, D. Wu, K. Cheng, X. Zhang, C. Chen, B. Liu, Y. He, *Nat. Commun.* **2014**, *5*, 1-9; b) Y. Liu, J. Liu, D. Chen, X. Wang, Z. Liu, H. Liu, L. Jiang, C. Wu, Y. Zou, *Macromolecules* **2019**, *52*, 5735-5740; c) D. Chen, I.-C. Wu, Z. Liu, Y. Tang, H. Chen, J. Yu, C. Wu, D. T. Chiu, *Chem. Sci.* **2017**, *8*, 3390-3398. d) B. Guo, J. Chen, N. Chen, E. Middha, S. Xu, Y. Pan, M. Wu, K. Li, C. Liu, B. Liu, *Adv. Mater.* **2019**, *31*, 1808355; e) C.-S. Ke, C.-C. Fang, J.-Y. Yan, P.-J. Tseng, J. R. Pyle, C.-P. Chen, S.-Y. Lin, J. Chen, X. Zhang, Y.-H. Chan, *ACS Nano* **2017**, *11*, 3166-3177; f) H.-Y. Liu, P.-J. Wu, S.-Y. Kuo, C.-P. Chen, E.-H. Chang, C.-Y. Wu, Y.-H. Chan, *J. Am. Chem. Soc.* **2015**, *137*, 10420-10429.
- [10] a) Z. Tao, G. Hong, C. Shinji, C. Chen, S. Diao, A. L. Antaris, B. Zhang, Y. Zou, H. Dai, *Angew. Chem. Int. Ed.* **2013**, *52*, 13002-13006; b) K. Shou, Y. Tang, H. Chen, S. Chen, L. Zhang, A. Zhang, Q. Fan, A. Yu, Z. Cheng, *Chem. Sci.* **2018**, *9*, 3105-3110.
- [11] Z. Zhang, X. Fang, Z. Liu, H. Liu, D. Chen, S. He, J. Zheng, B. Yang, W. Qin, X. Zhang, *Angew. Chem. Int. Ed.* **2019**, *59*, 3691-3698.
- [12] a) S. Albrecht, S. Janietz, W. Schindler, J. Frisch, J. Kurpiers, J. Kniepert, S. Inal, P. Pingel, K. Fostiropoulos, N. Koch, *J. Am. Chem. Soc.* **2012**, *134*, 14932-14944; b) J.-H. Dou, Y.-Q. Zheng, Z.-F. Yao, Z.-A. Yu, T. Lei, X. Shen, X.-Y. Luo, J. Sun, S.-D. Zhang, Y.-F. Ding, *J. Am. Chem. Soc.* **2015**, *137*, 15947-15956; c) T. Lei, X. Xia, J.-Y. Wang, C.-J. Liu, J. Pei, *J. Am. Chem. Soc.* **2014**, *136*, 2135-2141; d) J. Huang, Z. Gu, L. Zuo, T. Ye, H. Chen, *Sol. Energy* **2016**, *133*, 331-338.
- [13] Q. Zhang, M. A. Kelly, N. Bauer, W. You, *Acc. Chem. Res.* **2017**, *50*, 2401-2409.
- [14] a) F. Meyer, *Prog. Polym. Sci.* **2015**, *47*, 70-91; b) M. Kim, W.-T. Park, S. U. Ryu, S. Y. Son, J. Lee, T. J. Shin, Y.-Y. Noh, T. Park, *Chem. Mater.* **2019**, *31*, 4864-4872; c) M. Kim, W. T. Park, S. A. Park, C. W. Park, S. U. Ryu, D. H. Lee, Y. Y. Noh, T. Park, *Adv. Funct. Mater.* **2019**, *29*, 1805994.
- [15] Y. Zhang, J. Yu, M. E. Gallina, W. Sun, Y. Rong, D. T. Chiu, *Chem. Comm.* **2013**, *49*, 8256.
- [16] S. Zhu, Q. Yang, A. L. Antaris, J. Yue, Z. Ma, H. Wang, W. Huang, H. Wan, J. Wang, S. Diao, *Proc. Natl. Acad. Sci. U.S.A.* **2017**, *114*, 962-967.
- [17] R. Berger, G. Resnati, P. Metrangolo, E. Weber, J. Hulliger, *Chem. Soc. Rev.* **2011**, *40*, 3496-3508.
- [18] C. Wu, B. Bull, C. Szymanski, K. Christensen, J. McNeill, *ACS Nano* **2008**, *2*, 2415-2423.
- [19] Y. Hong, J. W. Lam, B. Z. Tang, *Chem. Comm.* **2009**, 4332-4353.
- [20] M. Cametti, B. Crousse, P. Metrangolo, R. Milani, G. Resnati, *Chem. Soc. Rev.* **2012**, *41*, 31-42.
- [21] W. Barford, M. Marcus, *J. Chem. Phys.* **2017**, *146*, 130902.
- [22] W.-C. Chen, P.-T. Chou, Y.-C. Cheng, *J. Phys. Chem. C* **2019**, *123*, 10225-10236.
- [23] G. S. M. Tong, K. T. Chan, X. Chang, C.-M. Che, *Chem. Sci.* **2015**, *6*, 3026-3037.
- [24] D. N. Louis, H. Ohgaki, O. D. Wiestler, W. K. Cavenee, P. C. Burger, A. Jouvett, B. W. Scheithauer, P. Kleihues, *Acta Neuropathol.* **2007**, *114*, 97-109.
- [25] C. Wu, S. J. Hansen, Q. Hou, J. Yu, M. Zeigler, Y. Jin, D. R. Burnham, J. D. McNeill, J. M. Olson, D. T. Chiu, *Angew. Chem. Int. Ed.* **2011**, *50*, 3430-3434.
- [26] Z. Yang, J. Chen, J. Yao, R. Lin, J. Meng, C. Liu, J. Yang, X. Li, L. Wang, L. Song, *Opt. Express* **2014**, *22*, 1500-1511.

Entry for the Table of Contents



Fluorination chemistry in semiconducting polymers resulted in highly bright polymer dots (QY=3.2%) in the NIR-II region. Followed by through-skull and through-scalp imaging of the mouse brain, the vascular morphology of transgenic brain tumors was quantitatively analyzed.